Dalton Transactions

ROYAL SOCIETY OF CHEMISTRY

PAPER

View Article Online
View Journal | View Issue

Cite this: *Dalton Trans.*, 2025, **54**, 8888

A study of simultaneous electrodeposition of Cu and S in choline chloride-ethylene glycol deep eutectic solvents: a pathway to the synthesis of copper sulfide hexagons†

Mateusz Szczerba, *[a,b] Joanna Kapusta-Kołodziej,[a] Mateusz M. Marzec, [c] Krystian Sokołowski [c] and Agnieszka Brzózka *[a]

Copper sulfides, with their tunable semiconductor properties, are promising materials for electronic and optoelectronic devices. Among the various synthesis techniques, electrodeposition stands out as a particularly effective method, offering precise control over the structure and composition of these compounds. In this study, we demonstrate the feasibility of co-electrodeposition of copper and sulfur on a carbon substrate using deep eutectic solvents (DESs) based on choline chloride and ethylene glycol. The effects of electrodeposition potential and electrochemical bath composition on the electroreduction process of $CuCl_2{\cdot}2H_2O$ and $Na_2S_2O_3$ mixtures in DESs were investigated. By controlling the electrochemical deposition parameters, we successfully obtained various structures, including Cu clusters, S-doped Cu clusters, and copper sulfide (Cu_xS) hexagons. The morphology and composition of the obtained materials were characterized using scanning electron microscopy (FE-SEM), energy dispersive X-ray spectroscopy (EDS), and X-ray photoelectron spectroscopy (XPS) techniques. Our findings indicate that co-electrodeposition of Cu and S requires potentials more negative than −0.84 V *vs.* Pt. Furthermore, the formation of Cu_xS hexagons was achieved by acidifying electrochemical baths with H_2SO_4. Interestingly, the electrodeposition of Cu from DESs was favored under all investigated synthesis conditions. Consequently, the average atomic percentage of S in the obtained Cu–S materials was a maximum of 9.36 at%, while EDS point analyses revealed that individual copper sulfide hexagons contained 22.7 to 23.8 at% of S. These results provide valuable insights into the co-electrodeposition of Cu and S from choline chloride-ethylene glycol DESs and pave the way for the future development of novel copper sulfide-based materials.

Received 11th March 2025,
Accepted 29th April 2025

DOI: 10.1039/d5dt00591d

rsc.li/dalton

1. Introduction

Transition metal sulfides (TMSs) have attracted considerable attention due to their unique electronic structure, intriguing properties, and consequent various applications in fields such as energy conversion, environmental remediation, and gas sensing.[1–3] Copper sulfides are particularly noteworthy among TMSs because of the abundant and easily accessible Cu resources, which makes the synthesis of Cu–S-based materials highly cost-effective.[4,5]

Copper sulfides are p-type semiconductors that exhibit remarkable versatility due to their ability to exist in a wide range of phases, from copper-rich Cu_2S to sulfur-rich CuS. The formation of various non-stoichiometric $Cu_{2-x}S$ compounds leads to a wide range of optical and electrical properties, enabling diverse applications.[6,7] These applications include photocatalysis, photoelectrocatalysis, and electrocatalysis,[8] as well as energy storage in supercapacitors.[9] Additionally, copper sulfides have shown utility in thermoelectric devices[10] and biomedicine.[11] The properties and potential applications of Cu–S materials are largely influenced by their composition and morphology and the form in which they are synthesized. These characteristics are, in turn, determined by the chosen synthetic method.[6]

Copper sulfides can be synthesized using different methods. Common methods include solvothermal[12] and

[a]*Department of Physical Chemistry and Electrochemistry, Faculty of Chemistry, Jagiellonian University, Gronostajowa 2, 30-387 Krakow, Poland.*
E-mail: mateusz_szczerba@doctoral.uj.edu.pl, agnieszka.brzozka@uj.edu.pl
[b]*Doctoral School of Exact and Natural Sciences, Jagiellonian University, Lojasiewicza 11, 30-348 Krakow, Poland*
[c]*Academic Centre for Materials and Nanotechnology, AGH University of Krakow, Av. Mickiewicza 30, 30-059 Krakow, Poland*

† Electronic supplementary information (ESI) available. See DOI: https://doi.org/10.1039/d5dt00591d

hydrothermal[13] processes, ion exchange reactions,[14,15] solid-phase synthesis,[16] and atomic layer deposition techniques.[17] Electrochemical deposition is another notable method for synthesizing Cu–S materials.[18–21] Electrodeposition has emerged as a powerful technique for synthesizing advanced materials, particularly transition metal sulfides, due to its ability to produce precisely controlled structures and compositions.[22] In this method, by applying an appropriate potential or current, the desired elements are directly deposited on the working electrode (current collector),[23] enabling the immediate application of the resulting material. The composition and morphology of the synthesized materials can be modified by adjusting not only the current/potential conditions but also other factors such as the synthesis temperature, precursor type and concentration, solvent choice, and electrolyte pH.[22,24,25] A key parameter in designing novel and complex structures is the selection of the solvent for the electrochemical bath. Recently, deep eutectic solvents (DESs) have gained considerable attention as environmentally friendly alternatives that hold great promise for electrochemical synthesis. DESs are particularly advantageous due to their wide electrochemical windows and high thermal stability, which distinguish them from traditional aqueous solvents.[25–27]

In recent years, many studies have focused on the electrodeposition of Cu-based materials using deep eutectic solvents. For example, Vukmirovic *et al.*[28] compared the electrodeposition of copper from ethaline-based baths on two different substrates: glassy carbon and platinum. These studies indicated that while the overall deposition behavior of Cu in DESs and aqueous media is similar, the charge and mass transfer rates differ substantially. Plaza-Mayoral *et al.*[29,30] investigated the electrodeposition of Cu–Au[29] and Cu–Ag[30] bimetallic nanostructures using reline-based baths. Their works demonstrated that the morphology, nanoparticle size, and elemental composition of the synthesized materials strongly depend on the applied potential and the composition of solutions used. Similar efforts have been made to study the co-electrodeposition of Cu with chalcogenides such as Te[31] and Se.[32] Catrangiu *et al.*[31] explored the electrodeposition of copper tellurides (Cu_xTe_y) from non-aqueous baths based on choline chloride and ethylene glycol, emphasizing the complexity of the process and the challenges in optimizing the synthesis parameters. In contrast, Sorgho *et al.*[32] focused on the formation of Cu_2Se structures using mixtures of Cu_2O and SeO_2 in reline-based solutions. Their research indicated that copper can be electrodeposited from DESs very readily, while electrodeposition of selenium requires much more negative potentials.

As demonstrated, the electrochemical deposition of copper-based binary structures from nonaqueous baths is a highly engaging and extensively researched topic in materials science. To the best of our knowledge, the co-electrodeposition of Cu and S from deep eutectic solvents has not yet been investigated. Therefore, in this study, we present a simple, one-step approach for synthesizing Cu–S structures by electrochemical deposition from environmentally friendly DESs based on choline chloride and ethylene glycol. To support our research, we provide a comprehensive electrochemical and physicochemical characterization of the solvents and baths used. We place particular emphasis on investigating the effects of the electrodeposition potential, as well as DES and electrolyte composition, on the properties of the resulting Cu and Cu–S materials. Importantly, we outline a systematic route for optimizing electrochemical synthesis parameters, highlighting the crucial role of bath acidification in achieving copper sulfide hexagons.

2. Experimental section

2.1. Materials

Choline chloride ($C_5H_{14}ClNO$, ≥98.0%) and sodium thiosulfate ($Na_2S_2O_3$, 99%) were purchased from Merck. Ethylene glycol ($C_2H_6O_2$, p.a.), copper(II) chloride dihydrate ($CuCl_2{\cdot}2H_2O$, ≥99.0%), sulfuric acid (H_2SO_4, 95%), and nitric acid (HNO_3, 65%) were purchased from Chempur. The water (H_2O) used in this study was purified using the Milli-Q® system. Carbon paper (180 μm in thickness) was purchased from Caplinq.

2.2. Instrumentation and software

IKA® C-MAG HS 7 magnetic stirrers with a temperature sensor were used to heat solvents and solutions. Kinematic viscosity measurements were performed using a ViscoClock plus viscometer from SI Analytics. For pH and conductivity measurements, a SevenDirect SD23 meter from Mettler Toledo was employed, equipped with an InLab® Science Pro-ISM pH electrode and an InLab® 731-ISM conductivity sensor. Electrochemical measurements were carried out using a BioLogic SP-300 or VMP-300 potentiostat, operated *via* EC-Lab® software. The morphology and chemical composition of the synthesized materials were examined using a field emission scanning electron microscope (FE-SEM/EDS, Hitachi S-4700 with a Noran system 7). X-ray photoelectron spectroscopy (XPS) analyses were performed with a PHI VersaProbeII scanning XPS system, utilizing monochromatic Al Kα (1486.6 eV) X-rays focused to a 100 μm spot. The photoelectron take-off angle was set to 45°, with pass energies of 117.50 eV for survey scans and 46.95 eV for the high resolution spectra acquisition. All XPS spectra were charge-referenced to the unfunctionalized, saturated carbon (C–C) C 1s peak at 285.0 eV. Deconvolution of the spectra was carried out using PHI MultiPak software (v.9.9.3) with the background subtracted using the Shirley method.

2.3. Preparation of deep eutectic solvents

In this study, three mixtures, composed of choline chloride (ChCl) and ethylene glycol (EG) mixed at different molar ratios, were used. Table 1 provides the abbreviated names (created for the purpose of the study) of all the obtained DESs, along with the corresponding ChCl : EG molar ratios. To obtain clear, colorless liquids, the mixtures of choline chloride

Table 1 Abbreviated names of the deep eutectic solvents (DESs) used, along with the corresponding molar ratios of choline chloride (ChCl) and ethylene glycol (EG) in the mixtures

Deep eutectic solvent name	ChCl : EG molar ratio
1_EG	1 : 1
2_EG	1 : 2
3_EG	1 : 3

and ethylene glycol were stirred for 12 h at 80 °C (1_EG DES), 60 °C (2_EG DES), and 40 °C (3_EG DES). At the given temperatures, the prepared mixtures became clear easily. Copper and sulfur precursor solutions were prepared analogously, using the appropriate DES as a solvent. All experiments were carried out using 50 mM $CuCl_2{\cdot}2H_2O$ and/or 50 mM $Na_2S_2O_3$, with the addition of 0, 25, or 50 mM H_2SO_4.

2.4. Cyclic voltammetry measurements

The electrochemical characteristics of selected deep eutectic solvents and solutions were investigated by performing cyclic voltammetry (CV) measurements in a three-electrode system. The glassy carbon disc electrode served as the working electrode, a platinum wire was used as the quasi-reference (Ref.) electrode, and a glassy carbon rod was used as the counter electrode. The use of a Pt quasi-reference electrode is a widely adopted approach in electrochemical studies of DESs due to its high thermal stability, ease of use, and compatibility with solutions containing significant amounts of Cl^- ions as well as acids.[33] Prior to each experiment, all electrodes were cleaned in a mixture of concentrated HNO_3 and H_2O in a 1 : 3 volume ratio. For mixtures of 50 mM $CuCl_2{\cdot}2H_2O$ and 50 mM $Na_2S_2O_3$ dissolved in 2_EG and 3_EG DES, the experiments were performed at 50–80 °C with a scan rate of 5 mV s^{-1} without stirring the electrolyte. For DESs (2_EG and 3_EG) and 50 mM solutions of individual Cu and S precursors, the experiments were performed in a similar manner, but at a single temperature, *i.e.*, 80 °C. In each case, the CV potential range was chosen based on the observed electrochemical stability of the electrolyte used.

2.5. Electrodeposition of Cu–S materials

Electrochemical deposition of Cu–S materials was performed in a three-electrode system, with carbon paper (CP) as the working electrode, a platinum wire as the quasi-reference electrode, and a glassy carbon rod as the counter electrode. Before electrodeposition, the CP electrodes were activated in a mixture of H_2O, H_2SO_4, and HNO_3 (volume ratio 1 : 1 : 1) at 60 °C for 6 h, followed by washing with water and drying at 60 °C under vacuum. The treatment introduces oxyl groups and surface defects within the carbon microfibers,[34] which may facilitate deposit nucleation. For each experiment, a fresh piece of carbon paper was used. The platinum wire and glassy carbon rod were cleaned in the same manner as that for the CV measurements. Electrodeposition was carried out at constant potentials of −0.84, −1.09, or −1.33 V at 80 °C for 10 min with continuous stirring of the electrolyte. The rationale behind the selection of electrodeposition potentials and the synthesis temperature will be discussed in Section 3.2. For the Cu–S synthesis, 12 mL of a solution containing a mixture of 50 mM $CuCl_2{\cdot}2H_2O$, 50 mM $Na_2S_2O_3$, and 0, 25 or 50 mM H_2SO_4 was used each time. During the study, we compared the electrodeposition process from electrolytes based on 2_EG DES (2_EG Cu–S baths) and 3_EG DES (3_EG Cu–S baths). 1_EG DES-based electrolytes were not investigated, which will be explained in Section 3.1. After synthesis, the samples were rinsed in warm water to remove impurities from the electrochemical bath.

3. Results and discussion

3.1. Physicochemical characteristics of solvents and solutions

Detailed physicochemical characterization was performed for the deep eutectic solvents used in the presented studies, as well as for the electrochemical baths prepared with them. This included determining kinematic viscosity (υ), conductivity (κ) and pH. The experiments were conducted over a wide range of temperatures (50–90 °C) or exclusively at 80 °C, which was the temperature selected for the electrodeposition of Cu–S materials. Fig. 1 illustrates the dependence of kinematic viscosity, conductivity, and pH on temperature for 1_EG, 2_EG and 3_EG DESs. As shown, for DESs containing an excess of ethylene glycol relative to choline chloride, measurements were conducted from 50 to 90 °C in 10 °C increments. Importantly, these solvents remained clear even at room temperature. Due to the low ethylene glycol content in 1_EG DES, experiments were not possible below 70 °C, as it was no longer clear under these conditions. Therefore, for 1_EG DES, the physicochemical characteristics were determined in a restricted temperature range (75–90 °C), in 5 °C steps.

The data presented in Fig. 1a–c demonstrate that temperature had a significant impact on the measured values of υ, κ, and pH. Among the studied solvents, 1_EG DES showed the highest viscosity (Fig. 1a), while 3_EG had the lowest. This difference is due to the variations in hydrogen bond strength between the solvent components.[35] Moreover, the differences between υ values, at a given temperature, were consistently smaller between 2_EG and 3_EG DES, compared to 1_EG DES, which showed significantly higher kinematic viscosity at both 80 and 90 °C. An increase in temperature resulted in a decrease in kinematic viscosity for all DESs, due to the breaking of hydrogen bonds between the components of the eutectic mixtures.[36,37] Conversely, conductivity exhibited a different trend (Fig. 1b). Throughout the entire temperature range, 3_EG DES exhibited the highest κ values, while 1_EG DES had the lowest. This behavior can be explained by the temperature-induced reduction in viscosity, which enhances the mobility of ions within the DESs, thereby increasing the overall conductivity.[37] Regarding temperature-related changes in pH (Fig. 1c), solvents with a lower ethylene glycol content consistently

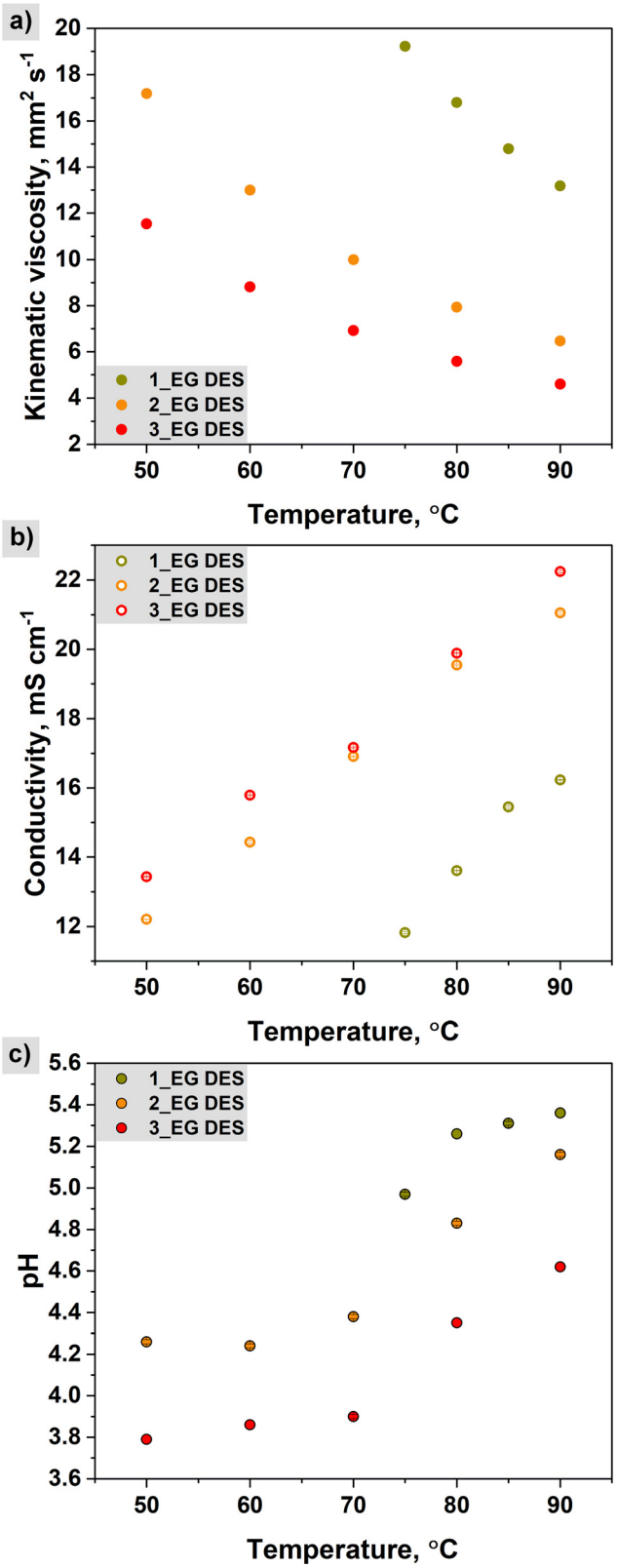

Fig. 1 The dependence of (a) kinematic viscosity, (b) conductivity, and (c) pH on temperature for 1_EG, 2_EG, and 3_EG deep eutectic solvents.

showed higher pH values, regardless of temperature. All the studied DESs were characterized by acidic pH values. For 2_EG and 3_EG DESs, lower temperatures (50–70 °C) resulted in minimal pH changes, with significant increases only observed at 80 and 90 °C. Similarly, 1_EG DES showed a notable increase as the temperature rose from 75 to 80 °C, with no significant variations observed at higher temperatures. These variations in acidity among the solvents are likely due to differences in the strength and quantity of hydrogen bonds between the mixture components, which in turn affected the acid–base equilibria.

Due to the limited operating temperature range for 1_EG DES, further studies focused exclusively on the other two solvents. Cu–S electrodeposition studies were conducted using solutions with a constant concentration of copper (50 mM $CuCl_2{\cdot}2H_2O$) and sulfur (50 mM $Na_2S_2O_3$) precursors. These mixtures were prepared in both 2_EG and 3_EG DESs and referred to as the 2_EG Cu–S bath and the 3_EG Cu–S bath, respectively. The Cu–S baths were acidified during subsequent adjustment by adding either 25 mM or 50 mM H_2SO_4. Fig. 2a illustrates the dependence of kinematic viscosity on temperature for the unacidified 2_EG Cu–S and 3_EG Cu–S baths, alongside the corresponding results for the original DESs. The effects of acid concentration ($C_{H_2SO_4}$) on the physicochemical properties of the Cu–S bath at 80 °C are shown in Fig. 2b–d.

From the analysis of the results illustrated in Fig. 2a, it can be seen that the addition of Cu and S precursors to the respective deep eutectic solvents had a minor effect on the observed kinematic viscosity values. At lower temperatures (50–60 °C), the inclusion of precursors caused slightly increased observed υ values, while at temperatures above 70 °C, the changes became negligible, particularly for the bath based on 3_EG DES. Similarly, the addition of H_2SO_4 did not significantly affect the measured values of kinematic viscosity (Fig. 2b) or conductivity (Fig. 2c). Conversely, the pH of the baths (Fig. 2d) showed significant changes. The unacidified mixtures exhibited a slightly alkaline pH ($7.5 < pH < 8.0$). The addition of acid, at both 25 and 50 mM concentrations, dramatically reduced the pH, resulting in strongly acidic baths ($0.3 < pH < 1.6$). Since electrochemical reactions (including electrodeposition) depend on a wide range of parameters, the results obtained will provide a better understanding of the processes taking place in the studied electrolytes. This matter will be discussed in the next sections.

3.2. Electrochemical properties of solvents and solutions

Before synthesizing Cu–S materials, the electrochemical characterization of baths containing the respective element precursors was carried out. To achieve this, cyclic voltammetry (CV) curves were recorded within the temperature range of 50–80 °C for a mixture of 50 mM $CuCl_2{\cdot}2H_2O$ and 50 mM $Na_2S_2O_3$ dissolved in 2_EG DES (Fig. 3a) and 3_EG DES (Fig. 3b). CV scans were recorded over a potential range of −0.90 to +1.80 V, starting with cathodic polarization from an initial potential of 0 V.

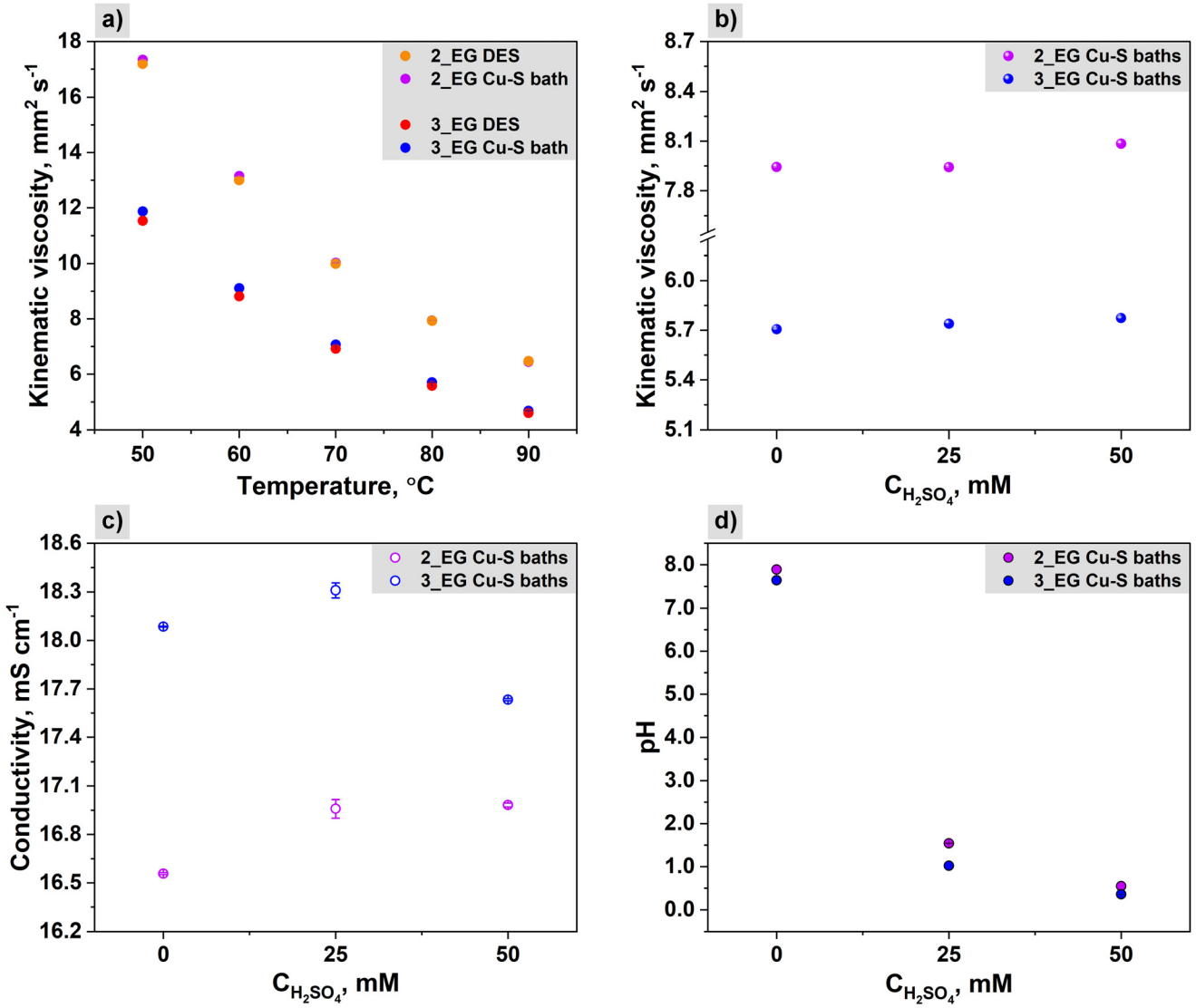

Fig. 2 (a) The dependence of kinematic viscosity on temperature for deep eutectic solvents (2_EG and 3_EG) and solutions containing a mixture of 50 mM $CuCl_2{\cdot}2H_2O$ and 50 mM $Na_2S_2O_3$ (2_EG Cu–S bath and 3_EG Cu–S bath). The dependence of (b) kinematic viscosity, (c) conductivity, and (d) pH on the concentration of H_2SO_4 in solutions containing a mixture of 50 mM $CuCl_2{\cdot}2H_2O$ and 50 mM $Na_2S_2O_3$ (2_EG Cu–S baths and 3_EG Cu–S baths).

The data presented in Fig. 3 demonstrate a significant effect of temperature on the current–potential dependencies. Higher temperatures generally lead to an increase in current density (J), likely due to the reduced kinematic viscosity and enhanced conductivity of the baths. Moreover, regardless of the temperature, rapid changes in J values, associated with electrolyte decomposition, were observed on both the cathodic and anodic sides within the potential range of the CV curves. Higher temperatures also accelerated the earlier decomposition of the electrolyte; however, some differences in the recorded curves for mixtures were observed. For the 2_EG Cu–S bath (Fig. 3a), the increase in cathodic current density at very negative potentials was less pronounced compared to that in the 3_EG Cu–S bath (Fig. 3b). Conversely, on the anodic side, the 3_EG Cu–S bath generally showed a slower increase in anodic current density at very positive potentials compared to the 2_EG bath. These observations are summarized in Table S1 of the ESI,† which presents a quantitative comparison of the current density values recorded at different potentials for the 2_EG Cu–S bath and the 3_EG Cu–S bath across all studied temperatures.

All recorded CV curves (Fig. 3) displayed two main reduction peaks, one of which appeared on the anodic side (just before E = 0 V) and was associated with the reduction of an oxidation product. At 50 °C, the most prominent reduction peak was observed at potentials of −0.95 and −0.90 V for the 2_EG Cu–S and the 3_EG Cu–S bath, respectively. In both cases, as the temperature increased, this peak became more pronounced, with its maximum shifting toward less negative potentials. Overall, increasing the temperature in the Cu–S

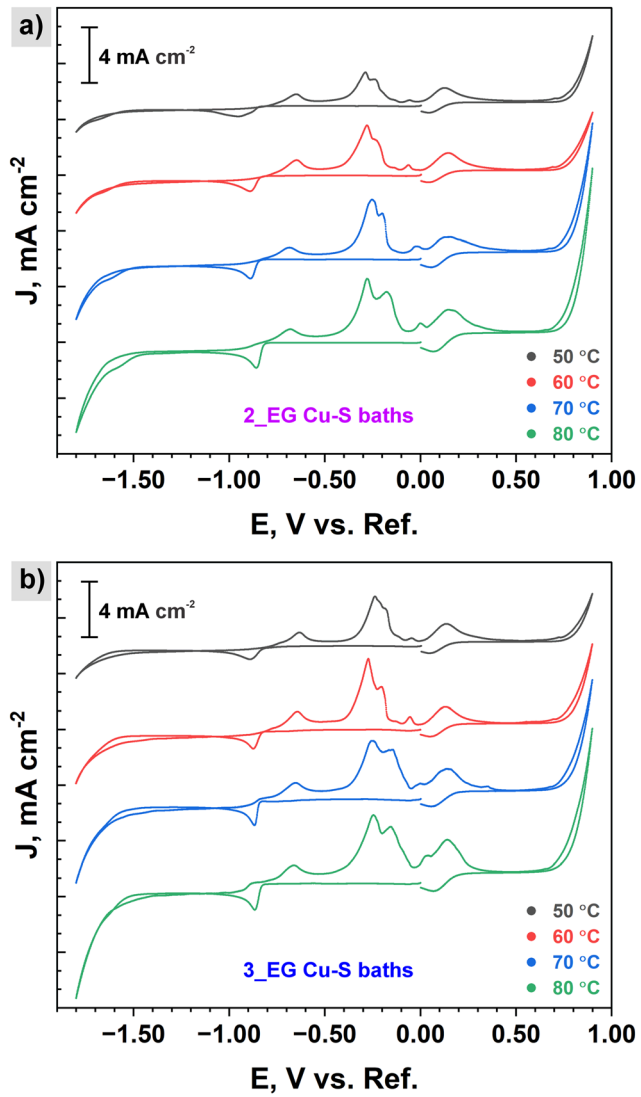

Fig. 3 Cyclic voltammetry curves recorded at 50–80 °C at a scan rate of 5 mV s^{-1} for a mixture of 50 mM $CuCl_2{\cdot}2H_2O$ and 50 mM $Na_2S_2O_3$ dissolved in (a) 2_EG DES and (b) 3_EG DES.

baths significantly promoted both electroreduction and electrooxidation of the precursors. Based on these findings, further investigations into the electrochemical characteristics of the solvents and solutions, as well as the electrodeposition of Cu–S materials, were conducted at 80 °C. Importantly, literature data indicate that both of the deep eutectic solvents used are thermally stable at the selected temperature,[38] which allows us to exclude the effect of their decomposition on the electrochemical reactions under investigation. Fig. 4 shows the cyclic voltammetry curves; the left-hand column displays the data for 2_EG DES and its corresponding baths, while the right-hand column presents the analogous data for 3_EG DES and its baths.

The CV curves presented in Fig. 4a and b confirm that neither of the selected solvents exhibited visible redox peaks or decomposition in the negative potential range (up to −1.80 V). Decomposition was only observed on the anodic side, which was irrelevant in the context of the planned studies, as the focus is on cathodic reduction regions for Cu–S electrodeposition. By analyzing the curves for single precursor baths (Fig. 4c–f), it can be seen that reduction peaks appeared in the studied potential range for both $CuCl_2{\cdot}2H_2O$ and $Na_2S_2O_3$ solutions. Interestingly, more intense peaks were observed for precursors dissolved in 3_EG DES. This is likely due to the lower viscosity of this solvent (Fig. 1a), which enhances ion mobility. For both solvents, the electroreduction of the copper precursor (Fig. 4c and d) followed a two-step mechanism ($Cu^{2+} \rightarrow Cu^{+} \rightarrow Cu^{0}$) as proposed by Vukmirovic *et al.*[28] When 2_EG DES was used, $CuCl_2{\cdot}2H_2O$ reduction peaks were observed at −0.23 V ($Cu^{2+} + e^{-} \rightarrow Cu^{+}$) and −1.40 V ($Cu^{+} + e^{-} \rightarrow Cu^{0}$). In contrast, for 3_EG DES, analogous peaks appeared at the less negative potentials of −0.20 and −1.26 V, respectively. For the sulfur precursor (Fig. 4e and f), a single characteristic reduction peak was observed, with a maximum located at −1.28 V for 2_EG DES and −1.31 V for 3_EG DES. The electroreduction of $Na_2S_2O_3$ was notably favorable in the less viscous DES, as evidenced by the prominent peak visible in Fig. 4f. It should be pointed out that literature data indicate that the two DESs differ in terms of intermolecular interactions. For 2_EG DES, most of the hydrogen bonds are formed between chloride anions and EG molecules, whereas in 3_EG DES, hydrogen bonding predominately takes place between EG molecules.[35] Solvents with different characteristics can influence interactions with copper and sulfur precursor ions, which in turn may directly affect the shape of the recorded cyclic voltamperograms. Our idea is supported by similar studies on the co-electrodeposition of SmCo films, where the ChCl : EG ratio influenced the position of characteristic redox peaks in the recorded CV curves.[39] Another key factor is the ability of Cu^{2+} ions to form complexes. For the DESs used, the main ligands coordinating Cu^{2+} are chloride ions (originating from $CuCl_2$ and choline chloride) and ethylene glycol molecules. A higher EG content can decrease the availability of free Cl^{-} ions while increasing the role of ethylene glycol in Cu^{2+} coordination, leading to changes in the geometry and stability of the complexes. Cu–Cl and Cu–EG complexes, in turn, may exhibit different redox potentials.[33,40,41] Furthermore, our data in Fig. 1 suggest that the solvents studied possess distinct physicochemical characteristics, reinforcing the likelihood of differences in electrochemical properties.

Comparing the CV curves for pure precursors (Fig. 4c–f) with those obtained for their mixtures (Fig. 4g and h) revealed significant differences. These differences included variation in the E values at which electrolyte decomposition became evident, as well as changes in the positions and number of redox peaks. For the Cu baths, decomposition on the anodic side occurred at less positive potentials, while the S baths remained stable up to 0.90 V. Conversely, on the cathodic side, $CuCl_2{\cdot}2H_2O$ solutions were stable up to −1.80 V, whereas $Na_2S_2O_3$ solutions began to decompose at less negative potentials. In the Cu–S baths, decomposition was observed on both the cathodic and anodic sides; however, the electrolytes

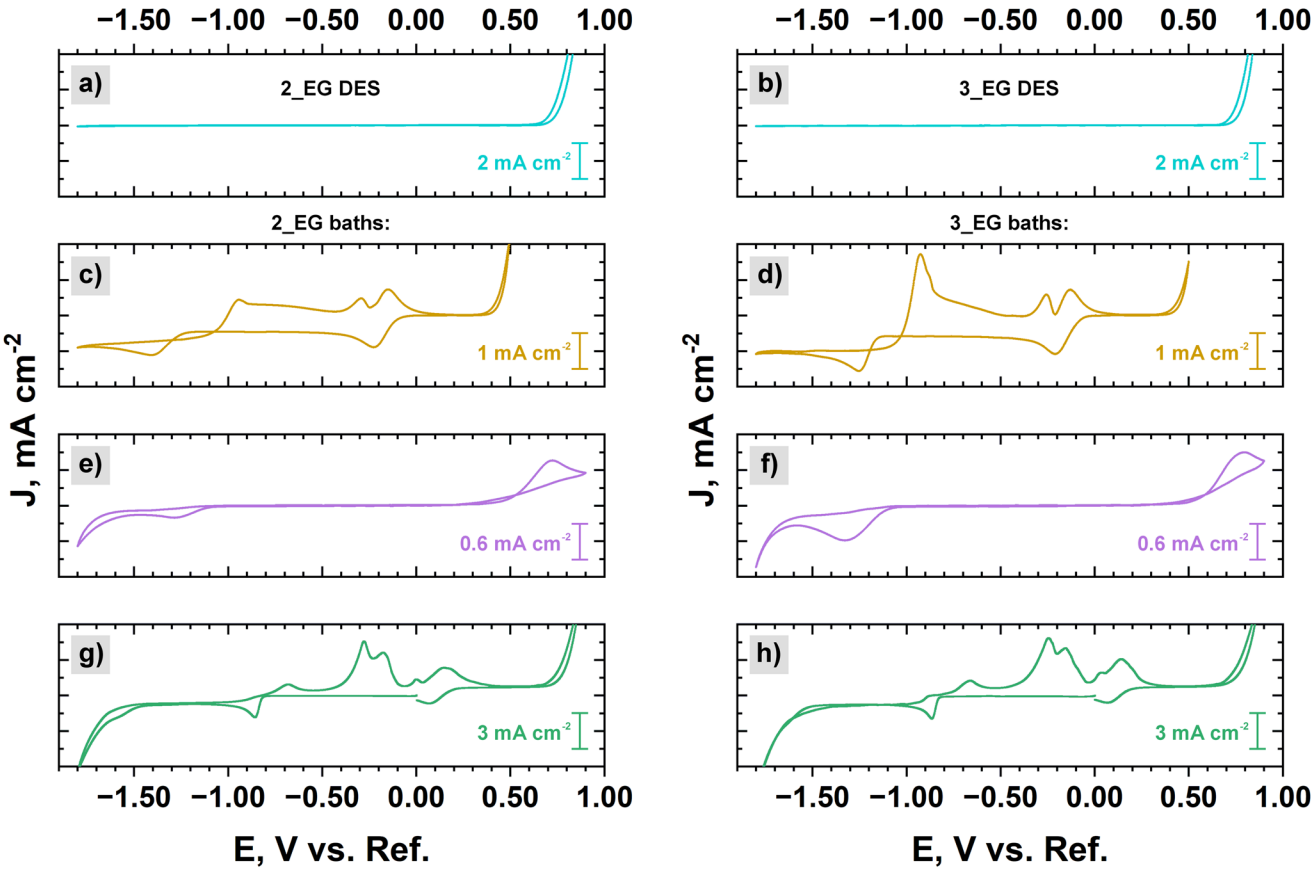

Fig. 4 Cyclic voltammetry curves recorded at 80 °C at a scan rate of 5 mV s^{-1} for (a) 2_EG DES and (b) 3_EG DES; 50 mM $CuCl_2{\cdot}2H_2O$ dissolved in (c) 2_EG DES and (d) 3_EG DES; 50 mM $Na_2S_2O_3$ dissolved in (e) 2_EG DES and (f) 3_EG DES; a mixture of 50 mM $CuCl_2{\cdot}2H_2O$ and 50 mM $Na_2S_2O_3$ dissolved in (g) 2_EG DES and (h) 3_EG DES.

demonstrated a relatively wide stability range. In turn, considering the redox peaks, it is evident that the electrochemical reactions occurring in the mixtures were significantly more complex than those in the pure precursor solutions. The main reduction peak for the Cu–S baths was observed at −0.84 V, with an additional peak (visible only for the 2_EG Cu–S bath) at −1.58 V. The analysis described in Section 3.3 identified the main peak (−0.84 V) as corresponding to the electroreduction of copper ions. Interestingly, the number of anodic peaks in the mixtures exceeded the sum of peaks observed for single precursors, further highlighting the complexity of the electrochemical processes in these systems. In addition to their distinct electrochemical characteristics, the analyzed electrolytes exhibited differences in color. $Na_2S_2O_3$ solutions were colorless, $CuCl_2{\cdot}2H_2O$ solutions were orange, while mixtures of both compounds had a green hue. These observations suggest that introducing $Na_2S_2O_3$ into $CuCl_2$ solutions influences the coordination of copper ions. $S_2O_3^{2-}$ ions can compete with Cl^- and EG ligands, forming various Cu–S_2O_3 complexes or mixed complexes with other ligands. Additionally, $S_2O_3^{2-}$ ions might stabilize the Cu^{1+} form of copper, analogous to aqueous solutions, thus broadening the range of possible complexes.[42,43] Taken together, these findings confirm that redox peak shifts in the cyclic voltammetry curves for solutions using different DESs are a natural occurrence and result from the intricate coordination chemistry of the studied systems.

Based on the CV data (Fig. 4g and h), the electrodeposition of Cu–S materials was initially planned at constant potentials of −0.84 and −1.58 V, *i.e.*, for values at which the characteristic reduction peaks discussed earlier were observed. However, preliminary experiments (data not included) revealed that the synthesis at −1.58 V was impractical due to the rapid decomposition of the electrolyte. Therefore, these conditions were abandoned, and two alternative potentials (*i.e.*, −1.09 and −1.33 V) located between −1.58 and −0.84 V were selected for future experiments. These newly chosen E values were within the regions of the electroreduction of Cu and S precursors in single-component electrolytes and offered greater stability for the electrodeposition process.

3.3. Study of Cu–S electrodeposition at different potentials

As described in the previous sections, the electrodeposition of Cu–S materials was carried out using a constant-potential method, with chronoamperometric (ChA) curves recorded during each experiment. The syntheses were conducted at 80 °C for 10 min, with continuous stirring of the electrolyte,

using carbon paper (CP) as the working electrode. The experiments began with Cu–S baths containing a mixture of 50 mM $CuCl_2{\cdot}2H_2O$ and 50 mM $Na_2S_2O_3$ dissolved in 2_EG and 3_EG DESs. Fig. 5a presents the ChA curves obtained during electrodeposition at different potentials (*i.e.*, −0.84, −1.09, and −1.33 V) from a Cu–S bath based on the 2_EG DES. Fig. 5b shows analogous curves for the electrosynthesis from the 3_EG Cu–S bath. Finally, Fig. 5c summarizes the average charge density (Q) values recorded during Cu–S electrodeposition at different potentials for electrolytes based on both DESs.

Analysis of the chronoamperometric curves presented in Fig. 5a and b reveals that the relationship between J and t varied depending on the electrodeposition potential, although certain common features were observed. One notable characteristic is the relatively rapid increase in cathodic current density, followed by a maximum value of J. The increase indicates the occurrence of an electrodeposition nucleation process, during which both the number and size of nuclei grow.[44,45] After reaching the maximum, the current density gradually decreases, followed by a plateau in the J *vs.* t curve. This stage corresponds to the ion diffusion-limited growth of the deposit.[46] A detailed analysis revealed that more negative deposition potentials result in the current density maximum being reached more quickly, suggesting faster nucleation and material growth.[30] Moreover, the maximum is achieved more rapidly for electrodeposition from the 3_EG Cu–S bath compared to the 2_EG bath, likely due to the lower viscosity and higher conductivity of the 3_EG solution (as shown in Fig. 2b and c). Additionally, higher J values at the maximum are associated with more negative potentials. This is typical and significantly influences the final characteristics of the synthesized materials.[29,44,47] Comparing the results shown in

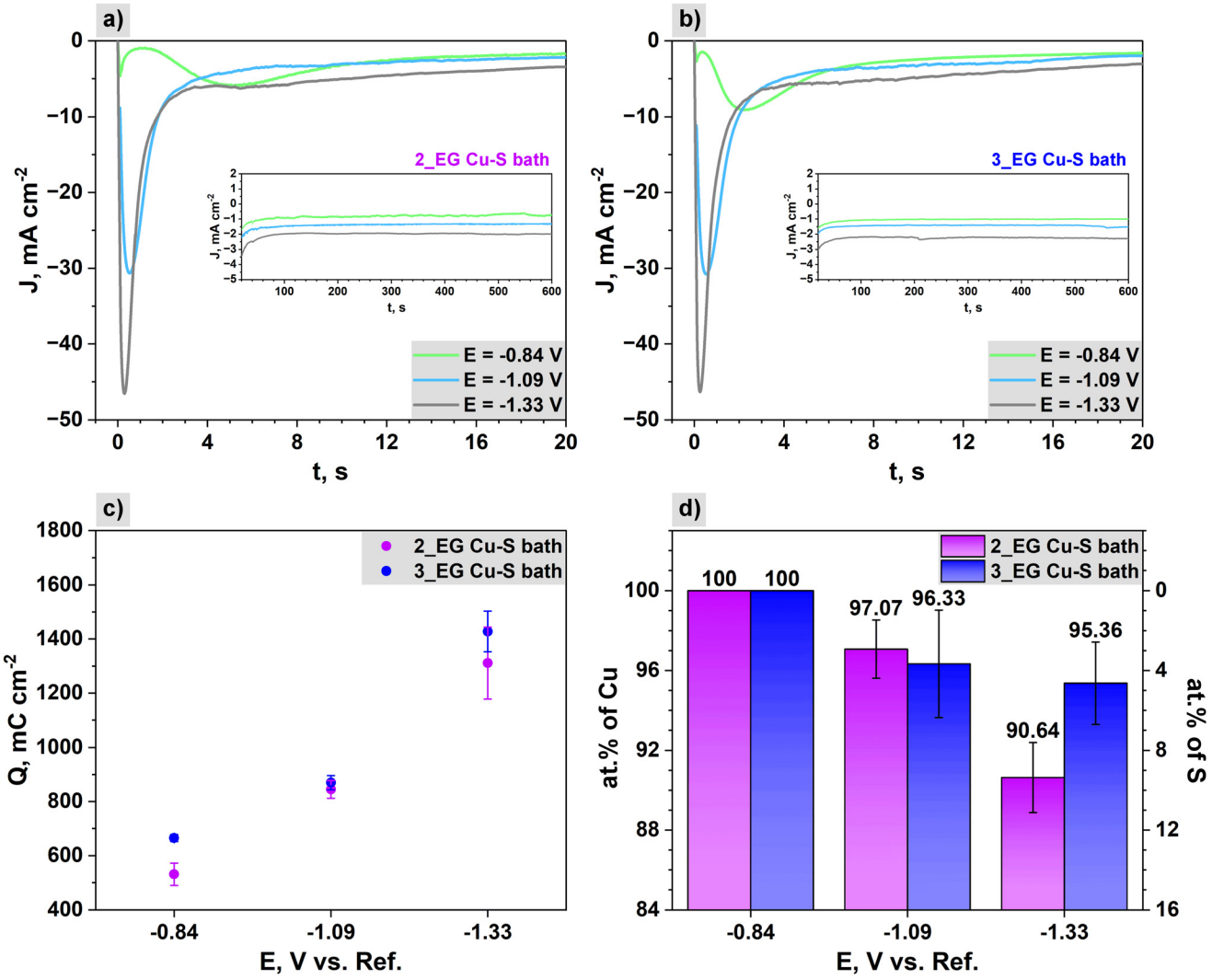

Fig. 5 Chronoamperometric curves recorded during the first 20 s of electrodeposition on carbon paper at different potentials (E), using a mixture of 50 mM $CuCl_2{\cdot}2H_2O$ and 50 mM $Na_2S_2O_3$ dissolved in (a) 2_EG DES and (b) 3_EG DES. The insets show the data for the remaining electrodeposition time (t). (c) Effect of the applied potential on the charge density (Q) recorded during Cu–S electrodeposition from the 2_EG Cu–S and 3_EG Cu–S baths. (d) Average atomic percentage (at%) of Cu and S in the electrodeposited materials.

Fig. 5a and b, it can be observed that the ChA curves obtained for the 2_EG Cu–S bath exhibit slightly lower current densities at the maximum, likely due to the higher viscosity and lower conductivity of the 2_EG solutions. After about 60 s of electrodeposition, nearly constant J values are observed across all curves, with higher cathode current densities recorded for syntheses at more negative potentials. This behavior influences the varying charge density (Q) values (see Fig. 5c), recorded during the electrochemical deposition. As expected, the data indicate that higher Q values correspond to more negative electrodeposition potentials and baths with higher conductivity, such as the 3_EG Cu–S bath. Interestingly, at a potential of −1.09 V, the Q values for both baths are remarkably similar, suggesting that similar electrochemical processes proceed under these conditions. However, the high standard deviations in Q values observed at −1.33 V indicate that deposition at this potential is less reproducible, likely due to excessive electroreduction of the electroactive species.

The electrodeposited materials were analyzed for their composition (energy dispersive X-ray spectroscopy, EDS) and morphology (scanning electron microscopy, FE-SEM). Fig. 5d summarizes quantitative EDS data indicating the average atomic percentage (at%) of copper and sulfur in the synthesized samples. The carbon content, corresponding to the CP substrate, was excluded from the calculations, with the assumption that Cu and S together account for 100% atomic composition. Detailed FE-SEM/EDS analyses for samples synthesized at specific potentials are shown in Fig. 6 (−0.84 V and −1.09 V) and Fig. S1, ESI† (−1.33 V).

As can be seen from Fig. 5d, copper was the primary component of the electrodeposited products, regardless of the electrodeposition potential or the Cu–S bath used. Notably, co-electrodeposition of Cu and S was only observed at potentials more negative than −0.84 V. EDS spectra (Fig. 6e) for samples synthesized at the least negative potential (*i.e.*, −0.84 V) did not show a typical K-line signal of sulfur, which would appear at the energy around 2.3 keV. This observation indicates that the reduction peak seen previously in the CV curves (Fig. 4g and h) at −0.84 V corresponds to the electroreduction of copper ions. Electrodeposition at more negative potentials resulted in Cu–S materials containing a small at% of S, with a higher S content observed at −1.33 V. These Cu–S materials exhibited distinct morphological differences compared to those consisting primarily of copper. Fig. 6a–e present FE-SEM images with corresponding EDS analyses for samples obtained at −0.84 V. Under these conditions, the electrodeposition process did not produce a continuous copper film over the carbon paper fibers. Instead, the 10 min synthesis led to the formation of Cu clusters distributed across different areas of the substrate. The electrodeposited materials displayed a complex morphology, indicative of a diffusion-controlled process.[46] Interestingly, using the 2_EG-based bath produced less morphologically regular and more aggregated copper clusters compared to the 3_EG bath. The characteristic dendritic morphology of copper clusters has previously been observed in both aqueous[48] and DES-based[49] solutions. In the presence of chlorides, the reduction of Cu^{2+} ions can proceed in steps ($Cu^{2+} \rightarrow CuCl \rightarrow Cu^0$), promoting the formation of Cu dendrites. The unique growth pattern of Cu during electrodeposition may result from surface saturation of the working electrode and limited mass transport, leading to irregular crystal growth development along preferential crystallographic directions.[48]

For electrodeposition at −1.09 V, as with −0.84 V, the resulting materials were not continuous films (Fig. 6f and i). The obtained EDS maps (Fig. 6g, h, j and k) further confirmed the co-electrodeposition of Cu and S in the same regions of the samples. Both baths produced morphologically similar Cu–S products, which, given the low at% of sulfur, can be described as S-doped Cu clusters. These clusters consisted of many smaller domains; however, due to their overlap, determining their average size was challenging. Electrodeposition at −1.33 V proved to be the most challenging. Under these conditions, excessive electroreduction of precursors occurred, resulting in a substantial amount of product that exhibited poor adhesion to the carbon substrate. After rinsing the samples in water, much of the deposit detached, making it difficult for FE-SEM/EDS analyses (Fig. S1, ESI†) to accurately reflect the true morphology and composition of the samples. Nevertheless, the results indicate that the most negative potential facilitated relatively uniform electrodeposition of the Cu–S material. However, as with the other cases, this process did not result in the formation of a continuous film.

3.4. Study of Cu–S electrodeposition from acidified electrochemical baths

Given the excessive Cu content in the obtained samples, further adjustment of the Cu–S electrodeposition process was undertaken to synthesize materials with a higher S content. A review of prior studies on the electrodeposition of metal sulfides from aqueous thiosulfate-containing electrolytes[18,50–53] highlighted the importance of preparing electrochemical baths with an acidic pH. In our case, the initial Cu–S baths had a slightly alkaline pH, ranging from 7.5 to 8.0 (Fig. 2a), which may have hindered the efficient co-electrodeposition of copper and sulfur. In aqueous systems, low pH leads to the disproportionation of $S_2O_3^{2-}$ ions into colloidal sulfur (S^0) and SO_3^{2-} ions.[50] Under such conditions, one probable electroreduction reaction is $S^0 \rightarrow S^{2-} + 2e^-$.[18] Although electrodeposition in non-aqueous solvents can differ significantly from that in aqueous systems, the effect of acidification on the composition and morphology of the deposited materials was investigated. Concentrated sulfuric acid was added to prepare Cu–S baths with low pH; the acid concentrations of 25 and 50 mM were chosen. The addition of acid altered the green colors of Cu–S baths to orange, similar to the orange solutions observed for pure $CuCl_2{\cdot}2H_2O$ in DESs. This color change may suggest a change in the complexation of copper ions. For subsequent experiments, an electrodeposition potential of −1.09 V was chosen, as this condition previously produced an adherent product with a composition containing both Cu and S. Syntheses were conducted at 80 °C for 10 min with constant

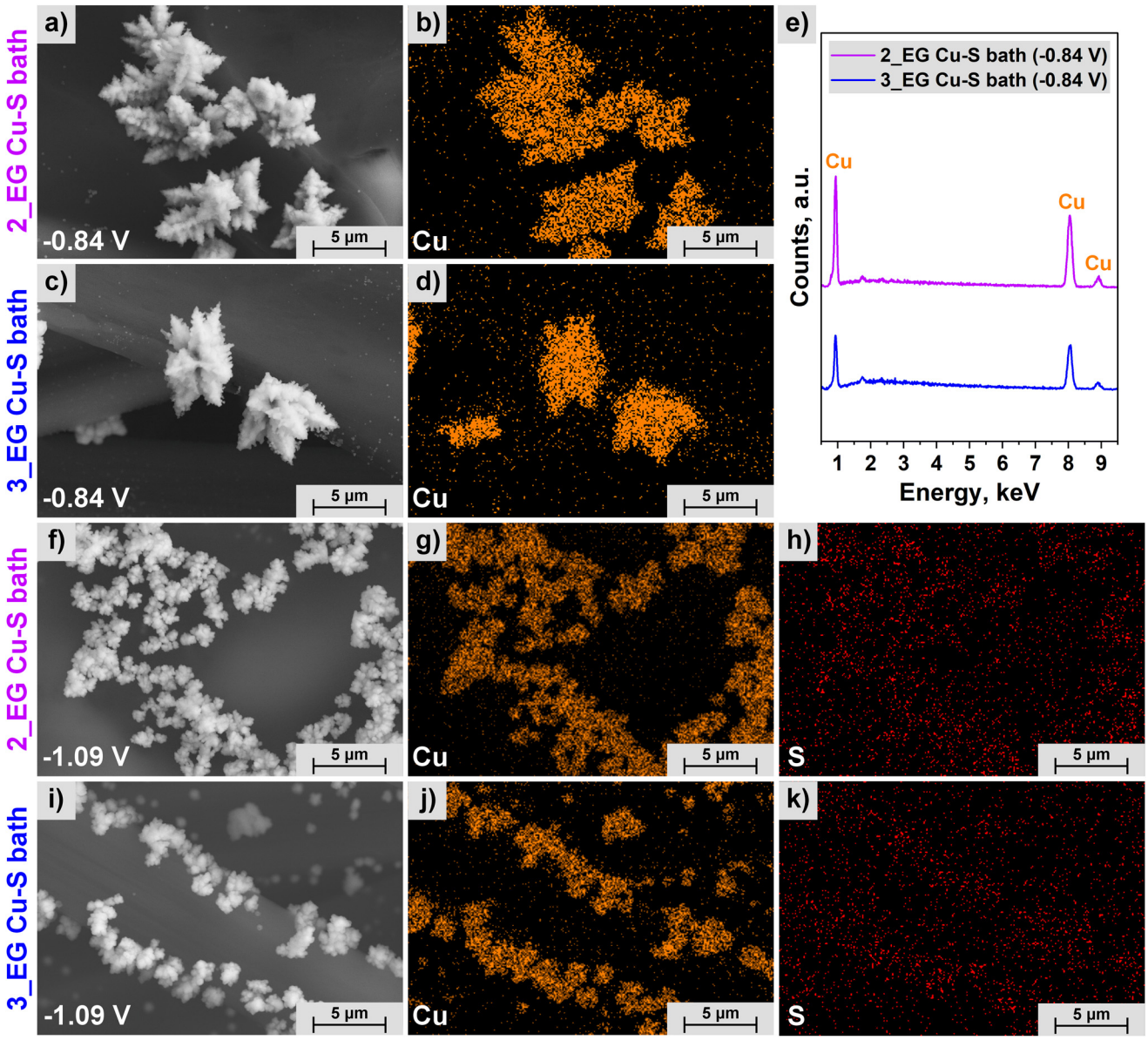

Fig. 6 (a) and (c) FE-SEM images and the corresponding (b) and (d) Cu EDS maps and (e) EDS spectra for samples synthesized at a potential of −0.84 V. (f) and (i) FE-SEM images and the corresponding (g) and (j) Cu and (h) and (k) S EDS maps for samples synthesized at a potential of −1.09 V. Results for samples electrodeposited from the 2_EG Cu–S bath (first and third lines) and the 3_EG Cu–S bath (second and fourth lines).

stirring of the electrolyte and using CP as the working electrode. Fig. 7a presents the ChA curves recorded during electrodeposition at −1.09 V from 2_EG Cu–S baths with the addition of 0, 25, or 50 mM H_2SO_4. Fig. 7b shows analogous curves recorded for electrodeposition from 3_EG Cu–S baths. Fig. 7c summarizes the average charge density (Q) values obtained during Cu–S electrodeposition from both 2_EG Cu–S and 3_EG Cu–S baths with different H_2SO_4 concentrations.

Within the ChA curves for the acidified solutions (Fig. 7a and b), an additional characteristic feature was observed. During the initial seconds of synthesis, a decrease in cathodic current density was evident, followed by an increase associated with the nucleation stage described earlier. The initial decrease in J values is attributed to the double layer charging process,[45] indicating a shift in the electrodeposition mechanism at −1.09 V. Furthermore, the presence of acid led to shallower minima in current density, while subsequent electrodeposition steps occurred at higher cathodic current densities compared to the acid-free baths. Comparing the curves for acid concentrations of 25 and 50 mM, it is evident that the higher acid concentration resulted in more negative J values, likely due to the increased number of highly mobile H^+ ions. Interestingly, the impact of the acid addition was particularly pronounced in the bath based on 3_EG DES, as highlighted by the charge density values (Fig. 7c). Higher concentrations of H_2SO_4 yielded higher Q values, although the increase was

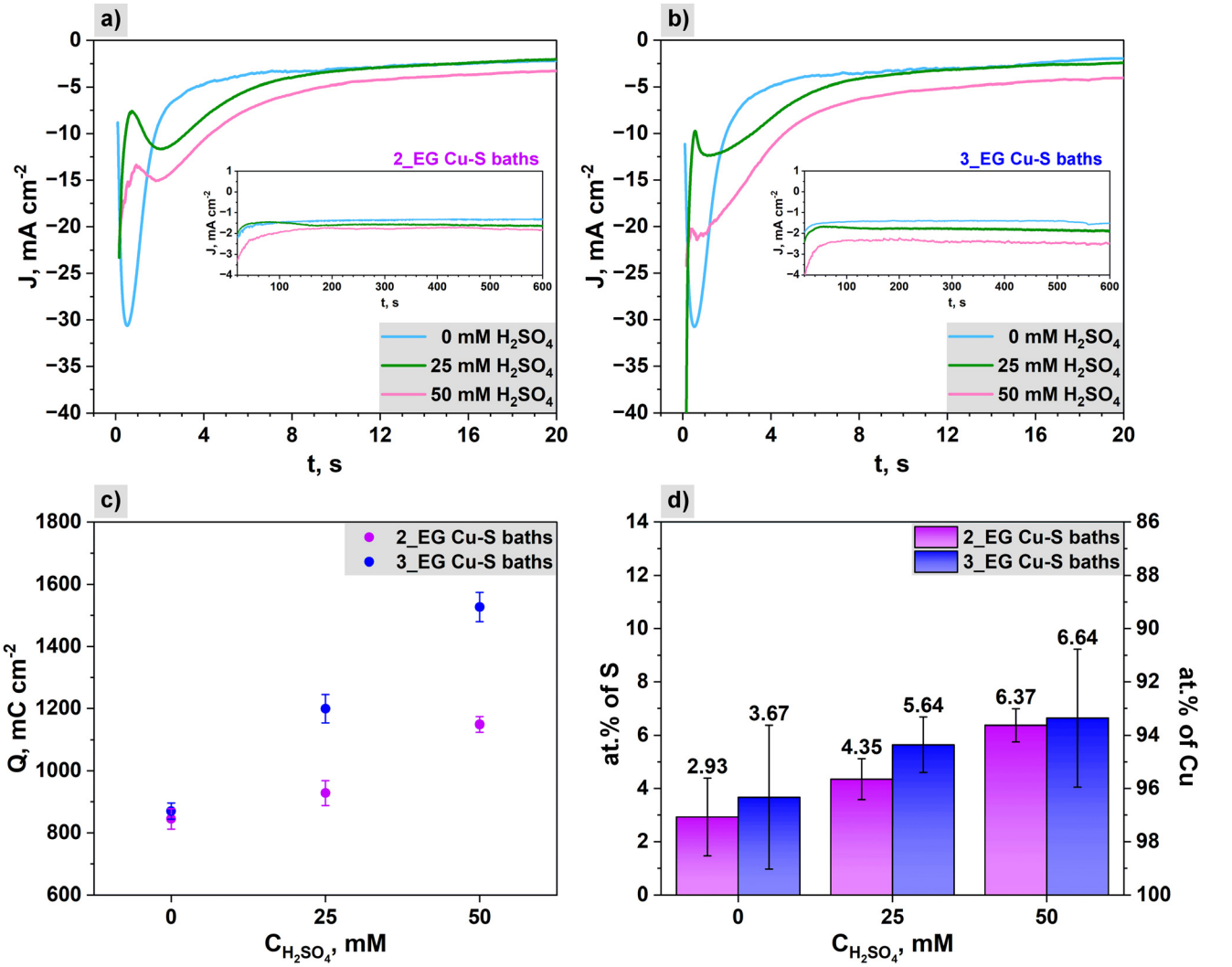

Fig. 7 Chronoamperometric curves recorded during the first 20 s of electrodeposition on carbon paper at a potential of −1.09 V using a mixture of 50 mM $CuCl_2{\cdot}2H_2O$ and 50 mM $Na_2S_2O_3$ with the addition of 0, 25, or 50 mM H_2SO_4 dissolved in (a) 2_EG DES and (b) 3_EG DES. The insets show the data for the remainder of the electrodeposition time (*t*). (c) Effect of H_2SO_4 concentration on the charge density (*Q*) recorded during Cu–S electrodeposition from 2_EG Cu–S and 3_EG Cu–S baths. (d) Average atomic percentage (at%) of S and Cu in the electrodeposited materials.

more significant for 3_EG Cu–S baths compared to the 2_EG Cu–S baths.

The samples obtained during electrodeposition at −1.09 V from different baths were examined in terms of morphology and composition using FE-SEM/EDS imaging. Fig. 7d summarizes quantitative EDS data, indicating the average atomic percentage (at%) of copper and sulfur in the synthesized materials. Fig. 8 provides detailed FE-SEM/EDS analyses for samples electrodeposited from baths containing 50 mM H_2SO_4. Analogous analyses for baths with 25 mM H_2SO_4 are summarized in Fig. S2, ESI.†

As shown in Fig. 7d, modifying the bath composition allowed an increase in the average S content of the materials; however, the maximum sulfur content achieved was only 6.64 at%, indicating that copper remained the predominant component of the deposits. The average atomic percentage of S was higher for materials synthesized from 3_EG Cu–S baths, with the sulfur content increasing with increasing H_2SO_4 concentration in the electrolyte. More notable than the average compositions were the FE-SEM images and the corresponding Cu and S EDS maps for the obtained samples (Fig. 8a–f and Fig. S2a–f, ESI†). Regardless of the electrodeposition conditions, two distinct types of structures were observed on the carbon substrate, appearing separately and not forming a continuous film. These differences are particularly illustrated in Fig. 8b, d, and f, where both copper-based clusters and hexagonal structures containing significant amounts of copper and sulfur are visible. Interestingly, the synthesis of similar hexagons has been previously reported in the literature as morphologies typical of various copper sulfides.[4,54,55] Given the previously described color change of the Cu–S baths, it may be inferred that different Cu–S_2O_3 complexes are present in the

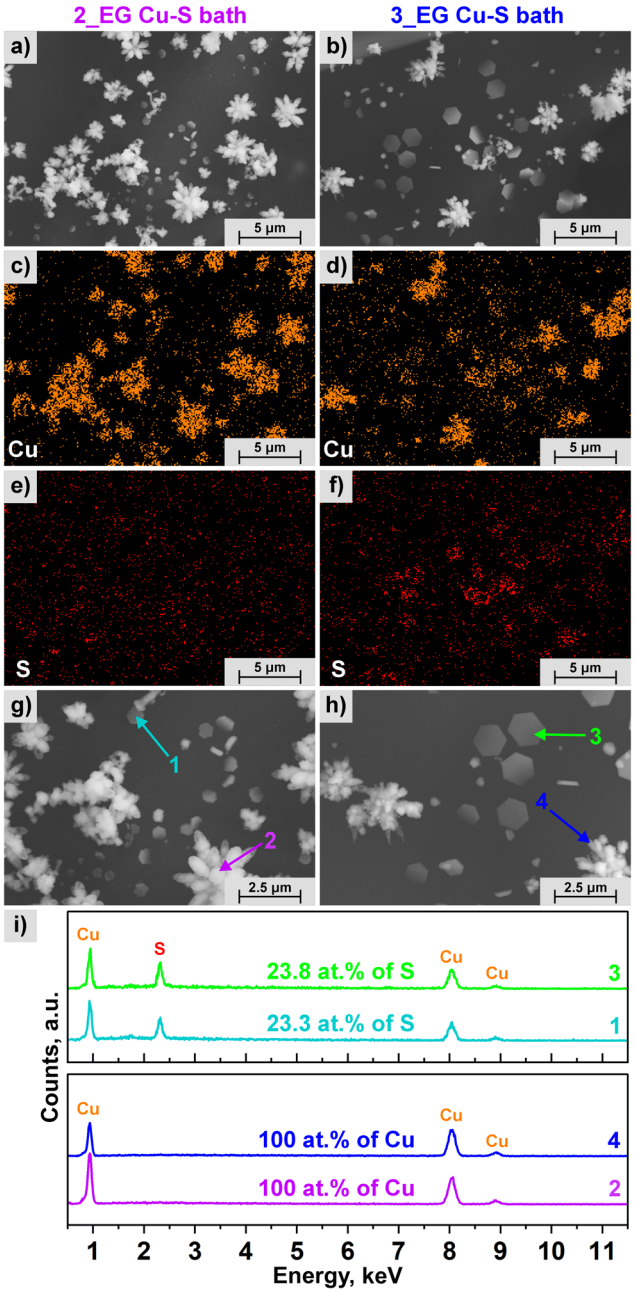

Fig. 8 (a) and (b) FE-SEM images and the corresponding (c) and (d) Cu and (e) and (f) S EDS maps for samples synthesized at a potential of −1.09 V from 2_EG Cu–S (the left-hand column) and 3_EG Cu–S (the right-hand column) baths acidified with 50 mM H_2SO_4 addition. (g) and (h) High magnification FE-SEM images with the corresponding (i) EDS point analyses.

electrolytes after acidification compared to before. This change likely leads to a change in the electrodeposition mechanism at −1.09 V. To further analyze these differentiated structures, higher magnification FE-SEM imaging and EDS point analyses were performed (Fig. 8g–i and Fig. S2g–i, ESI†). EDS spectra collected at points marked 1–4 revealed that the observed clusters were composed solely of Cu, whereas the hexagons contained both Cu and S, with the sulfur content ranging from 22.7 to 23.8 at% depending on the sample analyzed. The presented FE-SEM/EDS results suggest that the electrodeposition conditions used in this study successfully synthesized Cu-rich copper sulfide hexagons, which coexist alongside pure copper clusters. When comparing the morphologies of the samples obtained from the different baths, it is worth noting that the synthesis of hexagonal structures was more prevalent in 3_EG Cu–S baths. This may explain the significant increases in Q values (Fig. 7c) observed for these baths. In contrast, the 2_EG Cu–S baths yielded more copper clusters on the surface, with Cu–S structures present in lower quantities (compare Fig. 8a, b and Fig. S2a, b, ESI†). The Cu clusters were typically on the micrometer scale, while the individual hexagonal structures exhibited diagonals ranging from hundreds of nm up to about 1600 nm.

To further confirm the elemental composition and reveal chemical states, the selected samples were analyzed using the XPS technique. Fig. S3, ESI† shows the survey scans of Cu–S deposits synthesized at −1.09 V from the 3_EG Cu–S baths before and after H_2SO_4 acidification. The acquired XPS survey scans for both samples indicate that the same photoemission lines originate from copper, sulfur, oxygen, carbon and chlorine elements.[56] The detected C 1s, O 1s, and Cl 2p signals indicate the surface contamination of Cu–S samples from the Cu precursor, moisture, or from the chemisorption of oxygen-containing functionalities due to its exposure to air. Detailed information about the oxidation states of copper and sulfur was obtained from registered high-resolution XPS spectra. The curve-fitted high-resolution spectra acquired in the Cu $2p_{3/2}$, S 2p, and O 1s regions are shown in Fig. 9.

The Cu $2p_{3/2}$ spectra (Fig. 9a and d) were fitted with six components, with the first line at 932.7 eV corresponding to either the Cu^0 or the Cu^+ oxidation state like in Cu_2O and/or Cu_2S.[57–59] The spectra also exhibited shake-up structures in the binding energy range of 940–950 eV and an additional high left "shoulder", evidenced by the component centered at 934.5 eV, which suggests the presence of Cu^{2+} oxidation states.[57] The signal for Cu^{2+} is most likely associated with partial contamination of the samples by the copper precursor used in Cu–S electrodeposition. This interpretation is supported by the Cl 2p spectra (Fig. S4a and b, ESI†), which were fitted with a doublet structure (the $p_{3/2}$–$p_{1/2}$ separation equals 1.6 eV). The main $2p_{3/2}$ line is centered at 197.9 eV, indicating the presence of Cl^- ions from chlorides like $CuCl_2$.[56]

The S 2p spectra (Fig. 9b and e) showed two doublet structures with $2p_{3/2}$–$2p_{1/2}$ spin–orbit splitting of 1.16 eV. The first main $2p_{3/2}$ line observed at 161.7 eV is related to S^{2-} ions in copper sulfides (Cu_xS), as found in Cu_2S.[58] In contrast, the second $2p_{3/2}$ line observed at 168.3 eV originates from SO_4^{2-} ions.[60] The presented S 2p spectra reveal a significant difference between Cu–S samples synthesized without (Fig. 9b) and with (Fig. 9e) electrochemical bath acidification. As can be seen in Fig. 9b, in the absence of acid addition, sulfur co-electrodeposited with copper is prone to oxidation upon exposure to the air, which corresponds to low-intensity S^{2-} components.

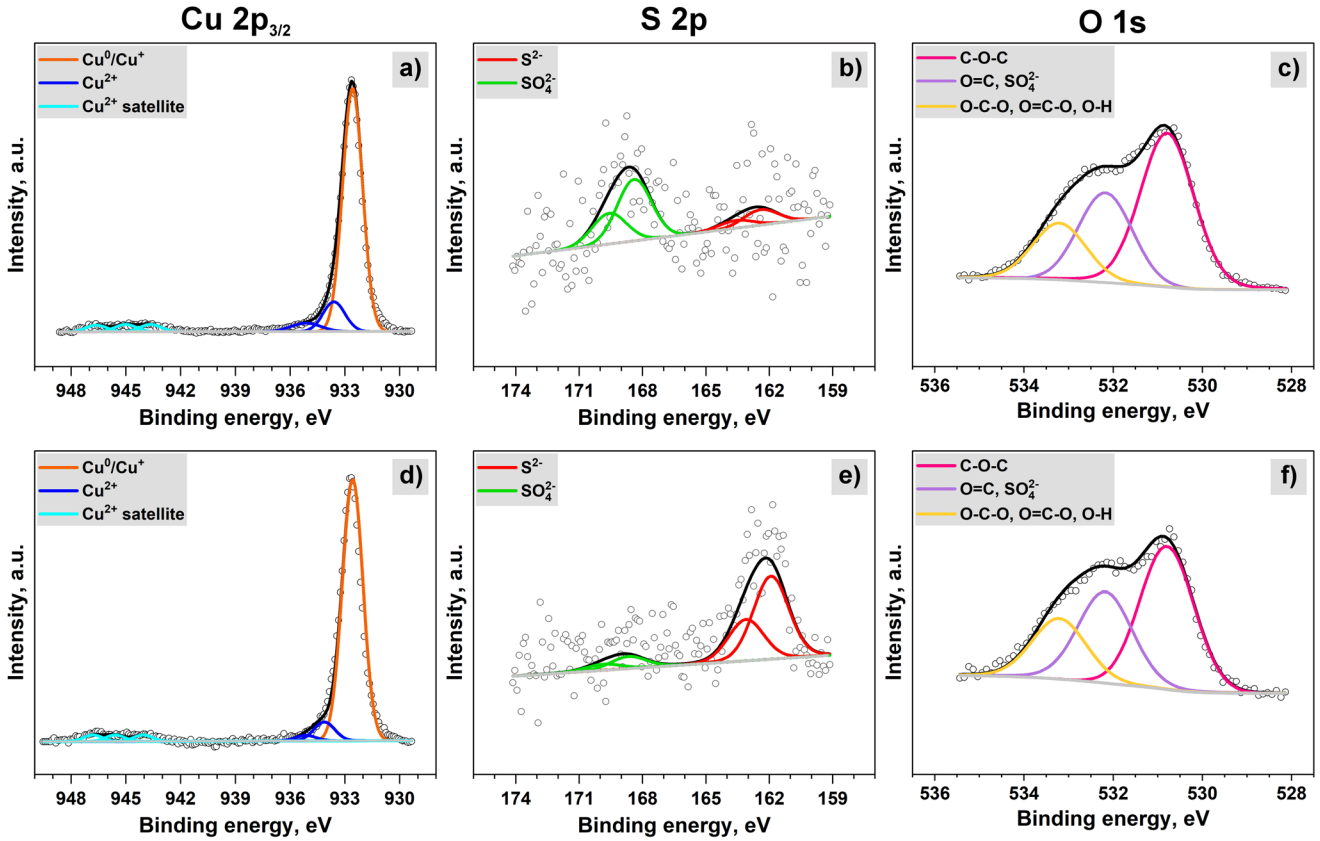

Fig. 9 High-resolution XPS spectra in the Cu $2p_{3/2}$, S 2p, and O 1s regions for Cu–S samples synthesized at a potential of –1.09 V from the 3_EG Cu–S bath (a)–(c) without and (d)–(f) with the addition of 50 mM H_2SO_4.

Conversely, the dominance of S^{2-} ions and the low detection of SO_4^{2-} (Fig. 9e) for Cu–S hexagons can suggest the formation of low air-sensitive Cu_xS-type compounds. In addition, the O 1s signal analysis (Fig. 9c and f) also indicates the presence of minor metal oxide species such as CuO or Cu_2O. The O 1s spectra were fitted with three components with the first line at 530.8 eV corresponding to C–O–C groups and/or the low part of O–Cu bonds. The second line at 532.3 eV indicates O=C type bonds and some part of O–S bonds. The third line at 533.2 eV corresponds to either O–C–O or –OH type species.[56,61,62] XPS analyses, supported by the earlier EDS analyses, indicate that the Cu–S structures electrodeposited from choline chloride and ethylene glycol-based deep eutectic solvents exhibit low sensitivity to air oxidation, which may be of interest for their future applications.

4. Conclusions

In this study, we present a simple, one-step electrodeposition method to synthesize various Cu and Cu–S structures using environmentally friendly deep eutectic solvents (DESs) composed of choline chloride and ethylene glycol. Based on the cyclic voltammetry curves recorded for the studied electrolytes, we selected the initial electrodeposition conditions. The chronoamperometry curves, in turn, allowed us to describe the mechanism of electrochemical deposition from $CuCl_2{\cdot}2H_2O$ and $Na_2S_2O_3$ mixtures prepared in DESs. By adjusting the electrodeposition conditions, we successfully produced Cu clusters, S-doped Cu clusters, and copper sulfide (Cu_xS) hexagons, as confirmed by characterizing the morphology and composition of the materials using FE-SEM, EDS, and XPS techniques. We believe that the presented results will enhance the understanding of Cu–S co-electrodeposition from DESs and pave the way for the development of new and complex copper sulfide-based materials.

Author contributions

Mateusz Szczerba: conceptualization, methodology, data curation, investigation, visualization, formal analysis, writing – original draft, and writing – review & editing. Joanna Kapusta-Kołodziej: data curation, investigation, and writing – review & editing. Mateusz M. Marzec: data curation, investigation, and writing – review & editing. Krystian Sokołowski: data curation, investigation, and writing – review & editing. Agnieszka Brzózka: conceptualization, methodology, data curation, investigation, funding acquisition, supervision, and writing – review & editing.

Data availability

The data supporting this article have been included as part of the ESI.†

Conflicts of interest

There are no conflicts of interest to declare.

Acknowledgements

This publication has been funded by the Anthropocene Priority Research Area budget under the program "Excellence Initiative – Research University" at the Jagiellonian University. The study was carried out using research infrastructure funded by the European Union in the framework of the Smart Growth Operational Programme, Measure 4.2; Grant No. POIR.04.02.00-00-D001/20, "ATOMIN 2.0 – Center for materials research on ATOMic scale for the INnovative economy". The FE-SEM imaging was performed in the Laboratory of Field Emission Scanning Electron Microscopy and Microanalysis at the Institute of Geological Sciences, Jagiellonian University, Poland.

References

1 S. Liu, Y. Li, X. Zhong, K. Yang, X. Li, W. Jin, H. Liu and R. Xie, *Small Struct.*, 2024, **5**, 2300536.
2 J. Di and W. Jiang, *Mater. Today Catal.*, 2023, **1**, 100001.
3 B. Chatterjee and A. Bandyopadhyay, *Mater. Sci. Eng., B*, 2023, **297**, 116781.
4 K. S. Bhat and H. S. Nagaraja, *J. Sci.:Adv. Mater. Devices*, 2020, **5**, 361–367.
5 S. Bonthula, S. R. Bonthula, R. Pothu, R. K. Srivastava, R. Boddula, A. B. Radwan and N. Al-Qahtani, *Sustainable Chem.*, 2023, **4**, 246–271.
6 P. Roy and S. K. Srivastava, *CrystEngComm*, 2015, **17**, 7801–7815.
7 B. He, K. Zhang and M. Zhu, *Green Energy Environ.*, 2025, **10**, 619–688.
8 C.-Q. Li and J.-J. Wang, *Small*, 2024, **20**, 2404798.
9 Z. Gan, X. Ren, M. Liu, M. Sun, W. Shen and Z. Li, *J. Energy Storage*, 2024, **99**, 113383.
10 P. Rawat and S. Kala, *Nano Express*, 2025, **6**, 012001.
11 Q. Wei, Y. Pan, Z. Zhang, S. Yan and Z. Li, *Chem. Eng. J.*, 2024, **483**, 149040.
12 M. Das, D. Das, R. Sk, S. Ghosh and P. P. Ray, *Opt. Mater.*, 2024, **156**, 115916.
13 A. Ait-karra, O. Zakir, A. Mourak, N. Elouakassi, A. Almaggoussi, R. Idouhli, A. Abouelfida, M. Khadiri and J. Benzakour, *J. Phys. Chem. Solids*, 2024, **185**, 111771.
14 Y.-I. Lee, *Mater. Chem. Phys.*, 2016, **180**, 104–113.
15 L. Chen, Z. Kong, H. Tao, H. Hu, J. Gao and G. Li, *Nanoscale*, 2022, **14**, 3907–3916.
16 E. Hwang, Y. Park, J. Kim, T. Paik and D.-H. Ha, *Nanomaterials*, 2021, **11**, 2317.
17 R. E. Agbenyeke, B. K. Park, T.-M. Chung, C. G. Kim and J. H. Han, *Appl. Surf. Sci.*, 2018, **456**, 501–506.
18 C. K. Kamaja, R. R. Devarapalli, Y. Dave, J. Debgupta and M. V. Shelke, *J. Power Sources*, 2016, **315**, 277–283.
19 J. Wang, Md. M. Rahman, C. Ge and J.-J. Lee, *J. Ind. Eng. Chem.*, 2018, **62**, 185–191.
20 G.-R. Xu, C. Ge, D. Liu, L. Jin, Y.-C. Li, T.-H. Zhang, Md. M. Rahman, X.-B. Li and W. Kim, *J. Electroanal. Chem.*, 2019, **847**, 113177.
21 A. Ait-karra, O. Zakir, A. Ait Baha, M. Lasri, R. Idouhli, M. Elyaagoubi, A. Abouelfida, M. Khadiri and J. Benzakour, *J. Solid State Electrochem.*, 2023, **27**, 2051–2065.
22 S. Mohapatra, H. T. Das, B. C. Tripathy and N. Das, *Chem. Rec.*, 2024, **24**, e202300220.
23 D. Piecha, M. Szczerba, R. Palowska, M. M. Marzec, K. Sokołowski, T. Uchacz, L. Liu, G. D. Sulka and A. Brzózka, *Appl. Surf. Sci.*, 2025, **684**, 161801.
24 M. Aliofkhazraei, F. C. Walsh, G. Zangari, H. Köçkar, M. Alper, C. Rizal, L. Magagnin, V. Protsenko, R. Arunachalam, A. Rezvanian, A. Moein, S. Assareh and M. H. Allahyarzadeh, *Appl. Surf. Sci. Adv.*, 2021, **6**, 100141.
25 A. Kityk, V. Pavlik and M. Hnatko, *Int. J. Hydrogen Energy*, 2023, **48**, 39823–39853.
26 A. P. Abbott, *Curr. Opin. Green Sustainable Chem.*, 2022, **36**, 100649.
27 S. Sugiarto, U. Aloka Weerasinghe, J. Kinyanjui Muiruri, A. Yu Qing Chai, J. Chee Chuan Yeo, G. Wang, Q. Zhu, X. Jun Loh, Z. Li and D. Kai, *Chem. Eng. J.*, 2024, **499**, 156177.
28 M. B. Vukmirovic, R. R. Adzic and R. Akolkar, *J. Phys. Chem. B*, 2020, **124**, 5465–5475.
29 E. Plaza-Mayoral, P. Sebastián-Pascual, K. N. Dalby, K. D. Jensen, I. Chorkendorff, H. Falsig and M. Escudero-Escribano, *Electrochim. Acta*, 2021, **398**, 139309.
30 E. Plaza-Mayoral, K. N. Dalby, H. Falsig, I. Chorkendorff, P. Sebastián-Pascual and M. Escudero-Escribano, *ChemElectroChem*, 2024, **11**, e202400094.
31 A.-S. Catrangiu, I. Sin, P. Prioteasa, A. Cotarta, A. Cojocaru, L. Anicai and T. Visan, *Thin Solid Films*, 2016, **611**, 88–100.
32 A. Sorgho, E. A. Mernissi Cherigui, M. Bougouma, F. K. Aldibaja, B. Nisol, F. Reniers, C. Buess-Herman and T. Doneux, *Electrochim. Acta*, 2022, **424**, 140676.
33 R. Bernasconi, M. Zebarjadi and L. Magagnin, *J. Electroanal. Chem.*, 2015, **758**, 163–169.
34 X. Wang, W. Li, D. Xiong, D. Y. Petrovykh and L. Liu, *Adv. Funct. Mater.*, 2016, **26**, 4067–4077.
35 H. Moradi and N. Farzi, *J. Mol. Liq.*, 2021, **339**, 116669.
36 K. A. Omar and R. Sadeghi, *J. Mol. Liq.*, 2022, **360**, 119524.
37 A. T. H. Yeow, A. Hayyan, M. Hayyan, M. Usman Mohd Junaidi, J. Saleh, W. Jefrey Basirun, M. Roslan Mohd Nor, W. Al Abdulmonem, M. Z. M. Salleh, F. Mohamed Zuki and M. Diana Hamid, *Results Chem.*, 2024, **7**, 101378.
38 A. Mero, S. Koutsoumpos, P. Giannios, I. Stavrakas, K. Moutzouris, A. Mezzetta and L. Guazzelli, *J. Mol. Liq.*, 2023, **377**, 121563.

39 G. Panzeri, M. Tresoldi, C. Rinaldi and L. Magagnin, *J. Electrochem. Soc.*, 2017, **164**, D930–D933.
40 E. Daskalopoulou, J. M. Hartley, R. M. Rivera, G. Zante and A. P. Abbott, *Phys. Chem. Chem. Phys.*, 2023, **25**, 4854–4861.
41 V. S. Cvetković, V. D. Jović, N. D. Nikolić, T. S. Barudžija, S. Dimitrijević and J. N. Jovićević, *J. Electroanal. Chem.*, 2024, **958**, 118161.
42 J. M. Mazurków, A. Kusior, E. Partyka-Jankowska and M. Radecka, *Cryst. Growth Des.*, 2024, **24**, 2475–2484.
43 G. Rábai and I. R. Epstein, *Inorg. Chem.*, 1992, **31**, 3239–3242.
44 Q. B. Zhang and Y. X. Hua, *Phys. Chem. Chem. Phys.*, 2014, **16**, 27088–27095.
45 Y. Yuan, G. Luo and N. Li, *RSC Adv.*, 2021, **11**, 31526–31532.
46 Z. Gao, Y. Jiang, Y. Meng, M. Du and F. Liu, *Molecules*, 2024, **29**, 5615.
47 I. Gavrilin, I. Martynova, I. Petukhov, I. Tsiniaikin, A. Pavlikov and S. Gavrilov, *J. Solid State Electrochem.*, 2024, **28**, 1521–1533.
48 W. Shao and G. Zangari, *J. Phys. Chem. C*, 2009, **113**, 10097–10102.
49 V. L. Filippov, N. I. Ponomarev, A. V. Shapagin, G. V. Kostikova and A. V. Rudnev, *Electrochim. Acta*, 2025, **525**, 146112.
50 K. Zarębska and M. Skompska, *Electrochim. Acta*, 2011, **56**, 5731–5739.
51 M. L. Madugu, O. I.-O. Olusola, O. K. Echendu, B. Kadem and I. M. Dharmadasa, *J. Electron. Mater.*, 2016, **45**, 2710–2717.
52 B. Altiokka and A. K. Yildirim, *J. Korean Phys. Soc.*, 2018, **72**, 687–691.
53 H. Lahmar, R. Kara, D. A. Hamza and A. Cherifi, *Phys. Status Solidi A*, 2024, **221**, 2300978.
54 D. Yoon, H. Jin, S. Ryu, S. Park, H. Baik, S. J. Oh, S. Haam, C. Joo and K. Lee, *CrystEngComm*, 2015, **17**, 4627–4631.
55 M. Senthilkumar and S. Moorthy Babu, *Mater. Sci. Semicond. Process.*, 2015, **40**, 203–208.
56 NIST X-ray photoelectron spectroscopy database, NIST standard reference database number 20, National Institute of Standards and Technology, Gaithersburg MD.
57 H.-J. Shen, H.-Y. Guo, S.-Y. Wen, L. Zhang, J.-J. Feng and A.-J. Wang, *ACS Appl. Nano Mater.*, 2024, **7**, 8113–8120.
58 B. Jana, D. Varghese, A. Narayan and A. Pandey, *J. Phys. Chem. C*, 2023, **127**, 8873–8879.
59 D. Zhao, B. Du, T. Li, C. Xu, Y. Li, Q. Yin, F. Wei, J. Qi and Y. Sui, *Appl. Surf. Sci.*, 2024, **674**, 160910.
60 M. Fantauzzi, B. Elsener, D. Atzei, A. Rigoldi and A. Rossi, *RSC Adv.*, 2015, **5**, 75953–75963.
61 M. C. Biesinger, B. P. Payne, A. P. Grosvenor, L. W. M. Lau, A. R. Gerson and R. St. C. Smart, *Appl. Surf. Sci.*, 2011, **257**, 2717–2730.
62 J. Liu, Y. Li, X. Jia, J. Shen, Y. Zhu and C. Li, *Small*, 2024, **21**, 2408279.